

## Six-port interferometer for W-band transceivers: design and characterization

Emilia Moldovan<sup>1</sup>, Nazih Khaddaj Mallat<sup>2</sup>, Serioja Ovidiu Tatu<sup>3</sup>

<sup>1,3</sup>Institut National de la Recherche Scientifique, Énergie Matériaux et Télécommunications, Canada

<sup>2</sup>College of Engineering, Al Ain University of Science and Technology (AAU), United Arab Emirates (UAE)

---

### Article Info

#### Article history:

Received Dec 3, 2018

Revised Mar 11, 2019

Accepted Mar 19, 2019

---

#### Keywords:

Couplers

Error analysis

Millimeter wave integrated circuits

Six-port technology

Wideband

---

### ABSTRACT

The study has presented an extensive analysis of an integrated millimeter wave six-port interferometer, operating over a 10 GHz band, from 80 to 90 GHz. It has covered both semi-licensed point-to-point links (81-86 GHz), and imaging sensor system frequencies (above 85 GHz). An in-house process is used to fabricate miniaturized hybrid millimeter wave integrated circuits on a very thin ceramic substrate. Two-port S-parameter measurements are performed on a minimum number of circuits integrated on the same die, exploiting the circuit's physical symmetry and chosen to collect enough data for full-port characterization. Based on these measurements on an integrated prototype, a six-port circuit computer model was implemented and advanced system simulations was performed for circuit analysis. Interferometer performances evaluated using several methods: analysis of harmonic balance, qi points<sup>2</sup>, homodyne quadrature demodulation, and error vector modulation (EVM). The analysis showed that this circuit could directly perform, without any calibration, the demodulation of various PSK and QAM signals over the 10 GHz band, with very good results.

Copyright © 2019 Institute of Advanced Engineering and Science.  
All rights reserved.

---

### Corresponding Author:

Nazih Khaddaj Mallat,  
College of Engineering,  
Al Ain University of Science and Technology,  
Al Ain, United Arab Emirates (UAE).  
Email: nazih.mallat@aau.ac.ae

---

## 1. INTRODUCTION

Nowadays millimeter wave components are requested more and more for very promising applications, such as multi-Gb/s wireless links, radar and imaging sensors. Six-ports have been used for decades in microwave bands and due to their well-known quadrature down-conversion and direct modulation applications; they also play an important role in millimeter wave transceiver implementation [1-14]. There is an increase in the use of microstrip antenna because of its lightweight, low fabrication costs, the capability of supporting multiple frequency bands, and integration with multiple input multiple output (MIMO) [6]. The disadvantages associated with this approach include; dielectric losses, surface wave losses, decreased gain, narrow bandwidth due to conductor losses, and large PCB structure [7].

The performance of any integrated circuit is dramatically improved if each component is carefully designed. It is particularly true for millimeter waves, where circuit dimensions are comparable to the guided wavelength. It has been demonstrated that microstrip technology can be successfully used at these frequencies by the appropriate choice of good quality, very thin substrate, transmission line characteristic impedances, and well-shaped components, despite the claims of some experts [11, 13]. The six-port interferometer was designed at a central frequency of 86 GHz to cover a 10 GHz band, from 80 to 90 GHz, due to the on-wafer S-parameter measurement capabilities of laboratory (60-90 GHz). This is the first Miniaturized Hybrid Microwave Integrated Circuit (MHMIC) six-port that operates at more than 80 GHz. The interferometer performances are analyzed using harmonic balance, qi points, quadrature demodulation for constellations up to 32 symbols, and EVM.

## 2. RESEARCH METHOD

The thinnest ceramic substrate on the market ( $127\ \mu\text{m}$ ) has been chosen for this study that ensures the successful wire-bonding of other integrated components, such as low noise amplifiers in a front-end design [13], and to have the narrowest possible microstrip lines. These lines are required to design closed shapes for couplers at this short guided wavelength ( $1.34\ \text{mm}$  at  $86\ \text{GHz}$ ). Considering its relative permittivity of 9.9 and according to the minimum width of a printed line in-house MHMIC process ( $50\ \mu\text{m}$ ), the maximum characteristic impedance of the microstrip line  $Z_0=74\ \Omega$  can be achieved. Therefore,  $Z_0$  values of  $35.36\ \Omega$  ( $w=248\ \mu\text{m}$ ),  $50\ \Omega$  ( $w=127\ \mu\text{m}$ ), and up to  $70.7\ \Omega$  ( $w=51\ \mu\text{m}$ ) can be used to obtain sufficient  $Z_0$  variation to design the required couplers.

The highest possible  $Z_0$  must be used to increase the quarter wavelength over the line width ratio as much as possible. In the best case, this ratio does not exceed 6. The worst-case ratio is only 1.35 at  $Z_0=35.36\ \Omega$ . This is a great challenge for designers who want to use the conventional shapes of these components or to keep the same nominal impedance for all circuits. In view of the above,  $50\ \Omega$  and  $70.7\ \Omega$  in designs were used in microstrip lines and tapered transitions for matching.

For S-parameter measurements with a two-port Vector Network Analyzer (VNA), the symmetry has been fully exploited to reduce the number of fabricated two-port circuits on a single ceramic die (size  $2.54\ \text{cm} \times 2.54\ \text{cm}$ ). A photograph of the complete MHMIC die is presented in Figure 1. For example, full S-parameter measurements of three-ports require two two-port printed circuits, three different circuits are needed for four-ports, and for the proposed six-port the measurements require seven different two-port printed circuits (instead of fifteen), due to its symmetry. All unused ports are loaded using integrated resistors of nominal impedance and RF short-circuits. Via-holes are avoided to reduce parasitic elements and to ensure the measurements' repeatability [15].

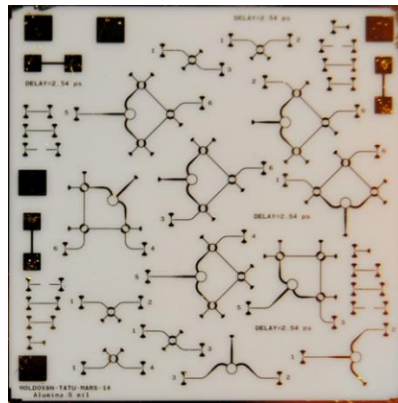


Figure 1. Photograph of MHMIC circuits on the ceramic die prepared for full-port S-parameter measurements (size  $2.54\ \text{cm} \times 2.54\ \text{cm}$ )

Figure 2 shows the photograph of the measurement set-up. It has been built in-house using equipment and parts from different manufacturers to best comply with the technical requirements. The set-up is mainly composed of a millimeter wave VNA and a high-precision manual probe station. The VNA includes the E 8362 PNA Network Analyzer and the N 5260A Millimeter Wave Head Controller from Keysight (Agilent) Technologies. Two-millimeter wave extenders, from OML Inc., optimized for Keysight (Agilent) N 5260A, are used for WR 12 waveguide operation. The huge attenuation on millimeter wave cables ensures very high dynamic range measurements.

The probe station is a modified Cascade Microtech Analytical probe station, Summit 9000. Two bent WR 12 waveguides are connected to millimeter wave extenders. Cascade Microtech Ground-Signal-Ground (GSG) wave guide probes having a pitch of  $150\ \mu\text{m}$  are used for measurements. A detail of the probe set-up, including a photo of MHMIC circuit under test, is presented in Figure 3. Focus Microwaves Inc fabricates the precision manual positioners. The positioners allow easy and accurate movements on three axes. The highest precision is on the Z-axis for probe landing, where sub- $0.1\ \mu\text{m}$  resolution is required.

The set-up includes an Olympus SZ61 stereo microscope equipped with a high-resolution Infinity 1 camera. The Infinity capture and the analyzing software allow the precise measurement of the circuits' physical dimensions, with around  $1\ \mu\text{m}$  resolution. Images are also displayed on a 32-inch LCD monitor to make probe positioning clearer.



Figure 2. Measurement set-up: millimeter wave probe station and VNA

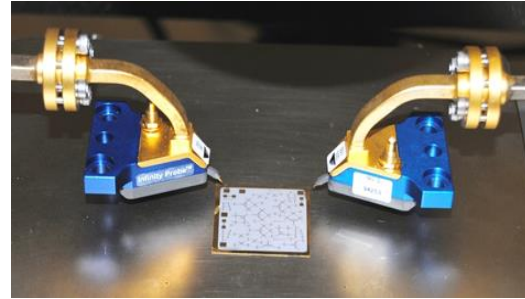


Figure 3. Measurement set-up: waveguide probes and MHMIC circuit under test

As usual, transitions to coplanar lines are adopted to perform VNA measurements using the probe station [15]. The layout of transitions used in the measurements, including the wideband RF load, is presented in Figure 4. The Thru-Reflect-Line (TRL) calibration kit is implemented on the same die. This is necessary for obtaining successful and repeatable calibration. Calibration using co-planar probes is very challenging at these high frequencies on the MHMIC prototype when the gold layer metallization is only  $1\ \mu\text{m}$  thick. Several TRL kits are printed, in case some are damaged by landing probes (i.e., scratched), as seen in Figure 1. The nominal impedance was chosen at  $70.7\ \Omega$ .

Repeatable measurements (magnitude and phase) require the same pressure to be maintained on probes and the probes to be landed at the same place at the co-planar inputs, from one two-port MHMIC to another. This is particularly important for measuring the transmission phase shift because these results will be used to implement the circuit computer models for system simulations. The two additional Cascade Microtech DC probes and a precision ohmmeter are used to measure contact resistance between coplanar probes and the gold plated transmission lines to keep the contact pressure at a constant and optimal value between one measurement and the next.

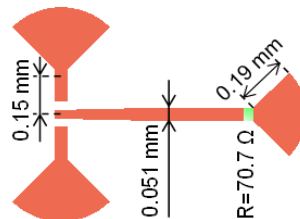


Figure 4. Layout of the microstrip to coplanar transition and wideband RF load

### 3. RESULTS AND ANALYSIS

#### 3.1. Wideband power divider/combiner

The circuit has been designed to correspond with the recent successful implementation at V-band [11]. The conventional design uses a T junction and short perpendicular transmission lines to connect the integrated resistor. The S-parameter performances of such a layout are very poor in millimeter waves, where discontinuities must be avoided.

The layouts of the proposed circuit, prepared for two-port measurements, are at the bottom right of Figure 1. The left one is prepared for the isolation measurements of the output ports; the right one is prepared for the transmission measurements. Figure 5 has presented the layout along with its basic dimensions. This rounded shape, with an overall circumference of six-quarter guided wavelengths (2.01 mm) and a corresponding  $740\ \mu\text{m}$  inner diameter, is ideal due to the short quarter wavelength over the line width ratio. The ring impedance is  $70.7\ \Omega$  ( $w = 51\ \mu\text{m}$ ) and the integrated resistor value is  $100\ \Omega$ .

The input signal is split, as in a conventional Wilkinson. The integrated resistor is connected with half-wavelength transmission lines having the same impedance of  $70.7\ \Omega$ . As seen, there are no steps or discontinuities, making the circuit ideal at millimeter wave frequencies. The tapered transitions to  $70.7\ \Omega$  are used to measure the S-parameters, according to the VNA calibration because the circuit ports are adapted to  $50\ \Omega$  as shown in Figure 1.

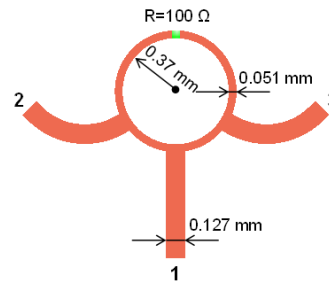


Figure 5. Layout of the wideband power divider/combiner.

In the present study, mainly the measurements and only the most important simulations have been displayed for S-parameters. As seen in Figure 6 the transmission magnitude is quite stable over 10 GHz. Additional insertion losses, as compared to simulation, are less than 1 dB. This is probably because the measurements are performed on the edge of the die; at port 2, the metallization was a little scratched during manufacture. Return losses at all ports are more than 20 dB as shown in Figure 7.

In addition, Figure 8 shows the excellent isolation between the output ports, demonstrating that the circuit is also a very good power combiner. This is particularly useful in power combining applications where the use of T junctions decreases return loss values and offers poor isolation between output ports 2 and 3 (as low as 6 dB for both parameters). Feeding networks of millimeter wave antenna arrays benefit from this circular layout, in particular [8, 13].

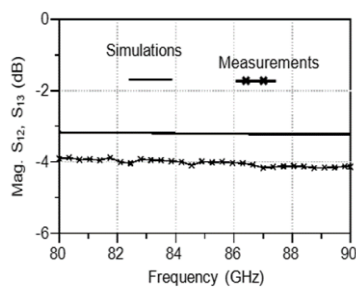


Figure 6. Transmission S-parameters: simulations and measurements

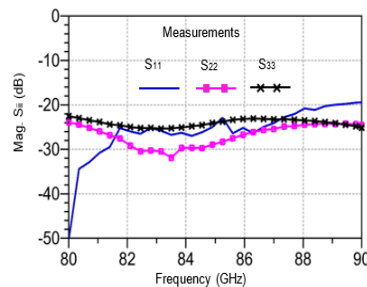


Figure 7. Return loss measurements at all ports

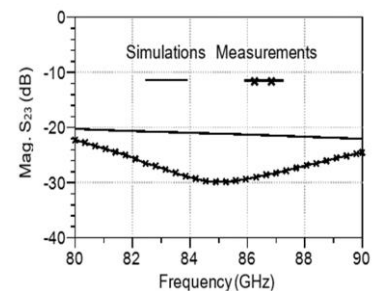


Figure 8. Isolation of output ports: simulations and measurements

### 3.2. Quadrature hybrid coupler

The millimeter wave quadrature hybrid coupler preserves the usual rounded shape of designs. The  $70.7 \Omega$  value has been chosen because the line width is too large for the commonly used  $50 \Omega$  characteristic impedance at ports. The integrated RF loads at unused ports are consequently equal to  $70.7 \Omega$ . Figure 9 shows its layout and main dimensions.

As seen at the bottom left of Figure 1, three measurement layouts are fabricated, corresponding to ports 1-2 and 1-3 for transmission, and 1-4 for isolation. Regarding the power divider, the additional insertion loss is less than 1 dB over the 10 GHz band as shown in Figure 10. Return losses are more than 16 dB at all ports as shown in Figure 11. The isolation between adjacent ports (1-4 and 2-3) is more than 20 dB over the whole band as shown in Figure 12. The phase shift kept almost  $90^\circ$  as shown in Figure 13. The phase shift of output ports represents an essential parameter for the analog signal processing of millimeter wave quadrature signals using the six-port.

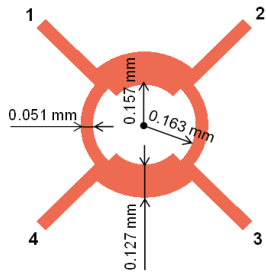


Figure 9. Layout of the quadrature hybrid coupler

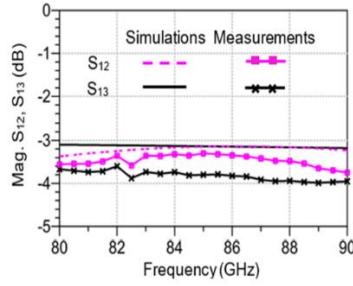


Figure 10. Transmission S-parameters: simulations and measurements

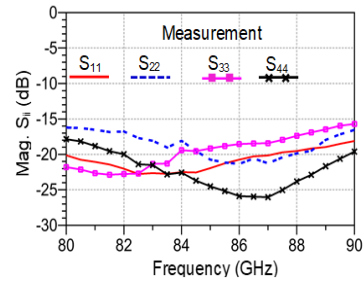


Figure 11. Return loss measurements at all ports

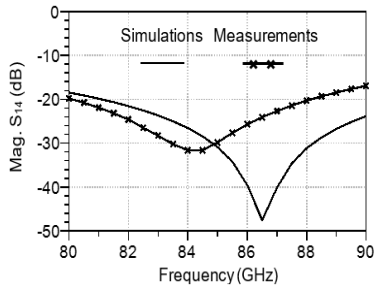


Figure 12. Isolation between adjacent ports of the hybrid coupler

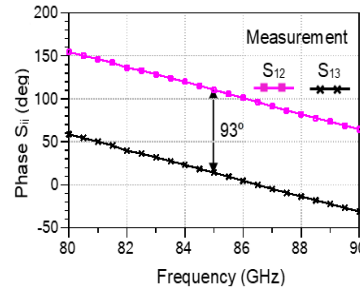


Figure 13. Phase measurements of transmission S-parameters

### 3.3. Six-port interferometer

The six-port interferometer is built using the previous two circuits; therefore, wideband behavior is expected. As explained, seven different six-ports have been implemented on the same ceramic die, along with other circuits as shown in Figure 1. This allows its complete S-parameter characterization. The layout and the outer dimensions of the six-port are shown in Figure 14. As usual in work, port 5 is the LO port, and port 6 is the input RF port. The circuit outputs are ports 1 to 4. Several of the most important S-parameters of the proposed six-port interferometer are plotted in Figures 15 to 22.

The return losses at RF input ports are higher than 17 dB on measurements as shown in Figure 15. The best results are obtained at port 6, the input of the modulated signals [10]. Excellent isolation between RF ports, of around 40 dB, has also been achieved at the central frequency as shown in Figure 16. This high isolation is a great advantage, compared to that achieved by conventional mixers, when the circuit is used as a direct quadrature demodulator [10]. Measured transmission magnitudes related to input port 6 show a variation of no more than 1 dB magnitude for all transmission parameters over 10 GHz bandwidth as shown in Figure 17. A quasi-linear phase variation with respect to 90° multiplies' differences is plotted in Figure 18. The phase difference between S61 and S62 is less than 2°, and the plots seem superposed.

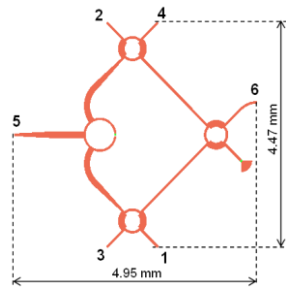


Figure 14. Layout of the six-port circuit

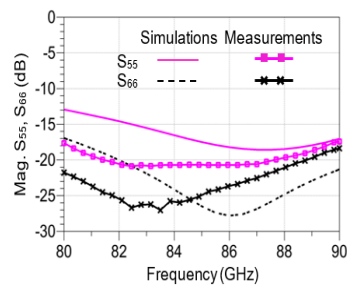


Figure 15. Return losses at input ports: simulations and measurements

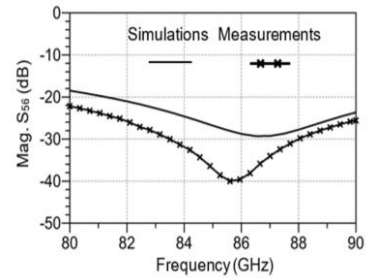


Figure 16. Isolation of input ports: simulations and measurements

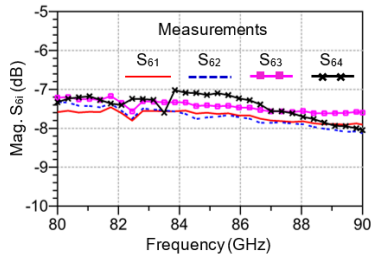


Figure 17. Transmission magnitudes between input RF port 6 and outputs

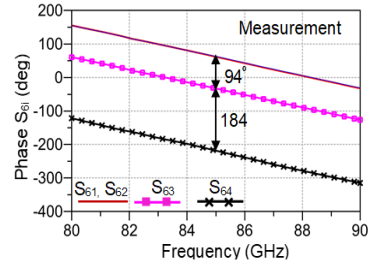


Figure 18. Transmission phases between input RF port 6 and the four outputs

It should be noted that a 4 μm probe positioning error corresponds to 1° of the transmission coefficient phase. A measurement error of a few degrees is reasonable, given that measurements are performed with two 150 μm probes on different circuits and given the size of the coplanar transition as shown in Figure 4. However, a maximum phase error of ± 2% concerning the central frequency is observed (fabrication and measurement errors included) over 10 GHz. Also, the overall transmission magnitude variation does not exceed 0.5 dB, from 80 GHz to 90 GHz at port 5 as shown in Figure 19. S51 is superposed to S54 and S52 is superposed to S53, due to the circuit symmetry as shown in Figure 14.

A quasi-linear phase variation of transmission coefficients with respect to 90° multiplies' differences is also to be seen in Figure 20. A maximum error of 1% is observed over 10 GHz. The measurement results of the return losses for the four output ports are shown in Figure 21. As can be seen, all ports are well matched in the considered frequency band. Typical nonadjacent isolation of the output ports, S12, is presented in Figure 22. The measurement result is very good, less than -20 dB in an 8 GHz frequency band. For adjacent ports, the results are similar to those shown in Figure12 for a 90° coupler.

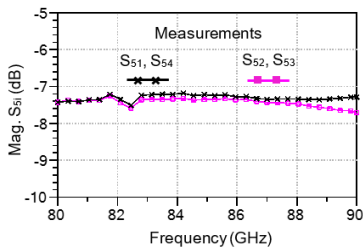


Figure 19. Transmissions' magnitudes between input RF port 5 and outputs

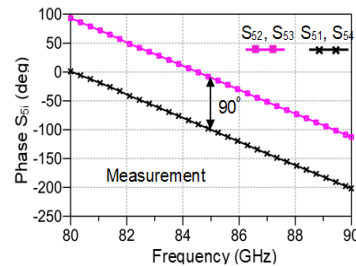


Figure 20. Transmission phases between input RF port 5 and the four outputs

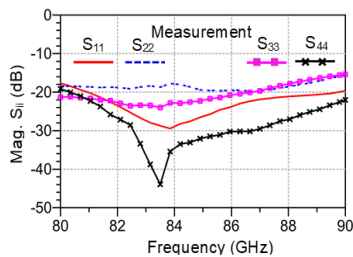


Figure 21. Return loss measurements of output ports

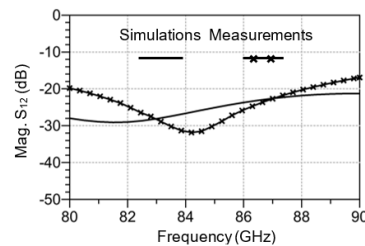


Figure 22. Typical simulation and measurement results of the outputs' isolation

A six-port interferometer model based on previous S-parameter measurements has been implemented in the Advanced Design System (ADS) software for further analysis. All two-port VNA S-parameter measurements of the MHMIC six-port are imported to ADS as data access components [15]. The performance of a six-port circuit is evaluated as an interferometer ted over the bandwidth using several global performance analyses: harmonic balance, the qi points, homodyne quadrature demodulation, and EVM because it is generally difficult to evaluate a six-port circuit using only S-parameters.

### 3.4. Harmonic balance

A harmonic balance analysis is performed as an initial design validation of the interferometric capabilities of the six-port circuit [7]. The block diagram of harmonic balance simulation is presented in figure 23. The millimeter wave signal generated by a local oscillator LO is split into two equal parts: the reference signal, injected at port 5, and the phase shifted one, injected at port 6. Ideal power detectors are connected to circuit outputs to highlight only the six-port performances. In practice, matched Schottky detectors are used [8, 13]. The output detected voltages  $V_i$  are read on load resistors  $R_{Li}$ . High-impedance loads are recommended.

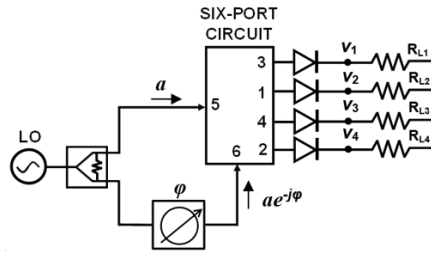


Figure 23. The harmonic balance simulation simplified block diagram

If phase  $\phi$  is swept over  $360^\circ$ , each output detects voltage varies as a shifted sinus function, as described in the two equations below [7, 10].

$$V_{3,1} = \frac{K}{2} a^2 [1 \pm \cos(\Delta\phi)] \tag{1}$$

$$V_{4,2} = \frac{K}{2} a^2 [1 \pm \sin(\Delta\phi)] \tag{2}$$

The constant  $K$  is related to power detector performances, and  $a$  is the magnitude of the normalized incident wave at RF input ports. As seen, sinusoidal functions are superposed over a DC value which is proportional to LO power. Two pairs of output detected voltages, one of ( $V_1, V_3$ ) and the other of ( $V_2, V_4$ ) are opposite in phase. The voltages of the even and odd index are in quadrature. In an ideal circuit, quadrature signals can be obtained using a differential function, at the same time reducing the DC offset to zero, as explained further in section IV C. Simulations using the measurement-based circuit model are performed over the 10 GHz band, and results are plotted in Figures 24 to 26. The LO power is set at 0 dBm for convenience and the phase is swept from  $0^\circ$  to  $360^\circ$ . The displayed waveforms having sinusoidal shapes are in good agreement with the previous theoretical equations. Minimum values are close to zero and are shifted by multiples of around  $90^\circ$ . The maximum values of all signals are almost the same.

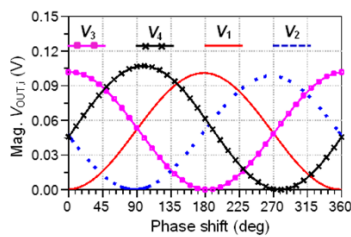


Figure 24. Magnitude of the power detected output voltages (85 GHz)

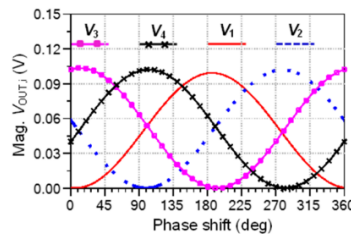


Figure 25. Magnitude of the power detected output voltages (80 GHz)

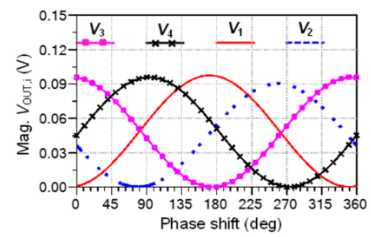


Figure 26. Magnitude of the power detected output voltages (90 GHz)

As mentioned, these values are obtained using measured S-parameters on different two-port circuits, as seen in Figure 1, phase errors are partly due to probe positioning, but also to slight physical dimensions and variations in load values from one two-port circuit to another. As compared to the values obtained for the central frequency, at the band edges that were considered, one 80 GHz and one 90 GHz, voltages are shifted by around  $\pm 10^\circ$ . This is easy to understand if the operating frequency changes are considered, but the physical dimensions remain the same.

The millimeter wave output signal of each port is an interferometric combination of two inputs. Therefore, slight magnitude variations after power detection are linked to the S-parameters (magnitude and phase), as plotted in Figures 17 to 20.

### 3.5. The $q_i$ points

From a historical point of view, the first six-port circuits were used as alternative, low-cost, vector analyzers [17-19]. In these designs, the power of one of the outputs is always proportional to the LO power. The other three detected output powers are function of the reflection coefficient of the device under test (DUT).

By definition, the  $q_i$  points are the values of the measured reflection coefficient which nulled the detected power at port  $i$ . For these circuits, the three  $q_i$  points are ideally spaced by  $120^\circ$  in the complex plane. To obtain the DUT reflection coefficient ( $\Gamma_L$ ), three circles having their center in the  $q_i$  points and their radiuses related to detected power are plotted.  $\Gamma_L$  is the intersection point of these circles [17].

By analogy, the  $q_i$  points for six-port receivers are defined as the normalized complex value of the input RF signal at port 6, which minimizes the measured power at the  $P_i$  outputs. If the input RF powers at ports 5 and 6 are equal, this minimal value would theoretically be equal to zero. Fast analog signal processing of millimeter wave signals, without any calibration, requires four  $q_i$  points spaced by  $90^\circ$  because there is no reference output power [6, 7, 10].

$$P_i = |aS_{5i} + ae^{-j\varphi}S_{6i}|^2 = |a|^2|S_{5i} + q_iS_{6i}|^2 \quad (3)$$

$$q_i = -\frac{S_{5i}}{S_{6i}}, i = 1, 2, 3, 4 \quad (4)$$

The four  $q_i$  point positions over the band, obtained using S-parameter measurements are presented in Figure 27. On the unit circle the ideal position of each point is marked by a dot. As seen, measurements of the circuit confirmed that the  $q_i$  points are separated by quasi  $90^\circ$  multiplies and are very close to the ideal values. A rotation movement of around  $20^\circ$  is observed from 80 GHz to 90 GHz. If the frequency is increased, the  $q_i$  points will rotate in a clockwise direction. This is in accordance with the previous harmonic balance results, and is mainly related to the variation of the electric length on transmission lines versus frequency. It should be noted that rotations are usually compensated in six-port receivers, as in all other phase shifts, due to the propagation or Doppler effects, by using a phase shifter at the LO port [20].

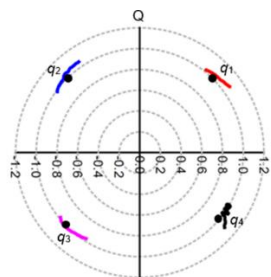


Figure 27. The  $q_i$  points position of the six-port over the 10 GHz band

### 3.6. PSK and QAM demodulation results

As demonstrated in [7], if the magnitude ratio of the input signals is equal to  $\alpha$ , the output detected voltages are:

$$V_{3,1} = \frac{K}{4}a^2[1 + \alpha^2 \pm 2\alpha\cos(\Delta\varphi)] \quad (5)$$

$$V_{4,2} = \frac{K}{4}a^2[1 + \alpha^2 \pm 2\alpha\sin(\Delta\varphi)] \quad (6)$$

The DC offset component can be eliminated in theory (dramatically reduced, in practice) by a differential approach:

$$I = V_3 - V_1 = \alpha Ka^2\cos(\Delta\varphi) \quad (7)$$

$$Q = V_4 - V_2 = \alpha Ka^2\sin(\Delta\varphi) \quad (8)$$

$$\Gamma = I + jQ = \alpha Ka^2\exp(j\Delta\varphi) \quad (9)$$

With the previous equations in mind, the basic demodulation diagram is shown in Figure 28. An additional gain is provided in the baseband module using differential amplifiers. The attenuator at port 6 can emulate the path loss of the millimeter wave wireless link. A phase shifter connected to one of the RF inputs can be used to rotate the demodulated constellation.

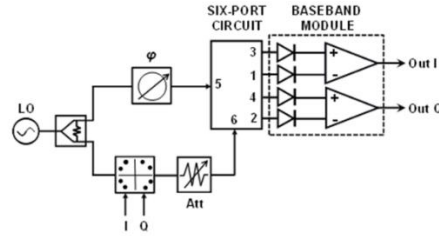


Figure 28. The demodulation simplified block diagram

The demodulator performances are evaluated by comparing, point by point, the position of each symbol, in the input complex plane (at the modulator level) with the position of the same symbol in the output complex plane (at the output of the baseband module). The power detector is considered ideal for highlighting only the characteristics of the six-port interferometer.

Supposing a perfect synchronism and no additional noise, Figures 29 to 33 show various demodulated constellations up to 32 symbols, with the six-port model based on S-parameter measurements in mind. The LO power is kept the same for all modulations, at -22 dBm, the additional attenuation at port 6 is 20 dB ( $\alpha = 0.1$ ), and the baseband module gain is 30 dB. All constellations are plotted at the central frequency. In order to better visualize the quadrature and position errors of the demodulated signals, symbols are transmitted in a certain order, for each modulation, and are linked by dotted lines. As noted at the beginning of section IV, the demodulation results show only the performances of the six-port circuit, and are used to evaluate its design and fabrication; they do not refer to an entire communication system.

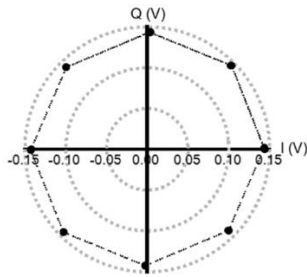


Figure 29. 8 PSK demodulation results

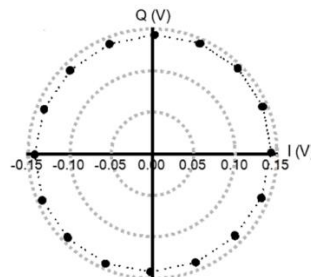


Figure 30. 16 PSK demodulation results

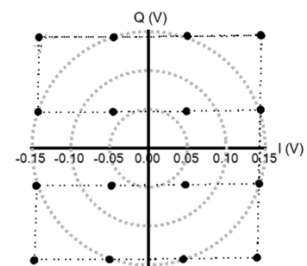


Figure 31. 16 QAM demodulation results

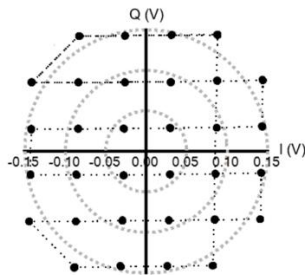


Figure 32. 32 QAM demodulation results

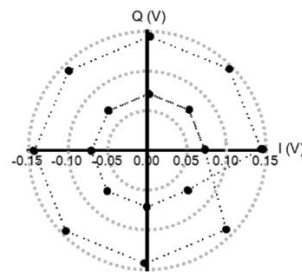


Figure 33. 16 symbols of the dual-ring demodulation results

As seen, the demodulation errors are barely visible to the naked eye. In the PSK modulations, the demodulated symbols are placed on circles. In the QAM modulation schemes, the points are equally spaced on the quadrature I and Q axes. Moreover, it can be observed that the symbols are also placed on three or five concentric circles in the case of 16 QAM and 32 QAM, respectively. With the available frequency band and this direct analog signal processing method, quasi-optical data-rates can be obtained at low-cost.

In practical wireless systems, additional white and phase noise is added and constellation points are grouped in clusters. Due to the huge bandwidth of several GHz, the white noise level is important. For example, if the band is increased from 100 MHz to 2 GHz (actual 4G to a future millimeter wave of 5G) additional 23 dB will be added to the noise level. In addition, the phase noise of millimeter wave oscillators is important because LO signals are usually obtained through frequency multiplication. Therefore, the number of symbols and the modulation scheme must be adjusted accordingly. For example, for 16 symbols, widely suggested as the maximum on millimeter wave 5G forums, the optimum modulation scheme is 16 QAM.

### 3.7. EVM results

Error vector magnitude represents the measurement of demodulator performances in the presence of impairments. The measured symbol location obtained after decimating the recovered waveform at the demodulator output is compared against the ideal symbol locations. The root-mean-square EVM and phase error are then used to determine the EVM measurement over N demodulated symbols.

In other words, the output demodulated constellation is compared point by point to the ideal constellation of the considered modulation scheme at the input of the modulator, with a real constant k used to normalize their sizes. As shown in Figure 34,  $k\Gamma_{IN,i}$  and  $\Gamma_{OUT,i}$  represent the ideal normalized and the measured symbol location, respectively. The resulting error vector is equal to the difference between the actual, as measured, and the ideal normalized symbol vectors. If all symbols are placed on a single circle (e.g. BPSK, QPSK, 8 PSK, and 16 PSK) the EVM can be mathematically expressed as:

$$EVM = \frac{\sqrt{\frac{1}{N} \sum_{i=1}^N |\Gamma_{OUT,i} - k\Gamma_{IN,i}|^2}}{|k\Gamma_{IN,i}|} \quad (10)$$

In this equation,  $\Gamma_{IN,i}$  is the *i*th ideal reference constellation point at the modulator input,  $\Gamma_{OUT,i}$  is the demodulated symbol, and N is the number of unique symbols in the constellation. It can be observed that  $|\Gamma_{IN,i}| = |\Gamma_{IN,max}|$ , because all symbols are located on a single circle. In order to use a similar equation for other modulation schemes, the EVM equation must be rewritten for each particular case. As can be seen in section C, the symbols can be considered as placed on concentric circles (two for dual-ring, three for 16 QAM, and five for 32 QAM) and their radiuses can be easily expressed in terms of one another.

All the symbols on the inner circles are projected to the exterior circle using the radius ratio factor, in order to evaluate all positioning errors in the same manner. Otherwise, the errors of symbols close to the origin are less important in EVM calculation if  $\Gamma_{IN,max}$  is considered in the denominator of (10), as is often the case. For example, in the case of the dual-ring constellation, the sixteen symbols are placed on two concentric circles, with a ratio of  $R_2 / R_1 = 2$  between radiuses. If the number of symbols  $N = 16$ , the first 8 symbols on the inner circle (radius  $R_1$ ) and the other 8 on the outer circle (radius  $R_2$ ), the constant k can be calculated as follows:

$$k = \frac{\frac{1}{16} \left( \frac{R_2}{R_1} \sum_{i=1}^8 |\Gamma_{OUT,i}| + \sum_{i=9}^{16} |\Gamma_{OUT,i}| \right)}{|\Gamma_{IN,max}|} \quad (11)$$

Consequently, if (9) is the EVM equation for these 16 symbols, the dual-ring constellation becomes:

$$EVM = \frac{\sqrt{\frac{1}{16} \left( \sum_{i=1}^8 \left| \frac{R_2}{R_1} (\Gamma_{OUT,i} - k\Gamma_{IN,i}) \right|^2 + \sum_{i=9}^{16} |\Gamma_{OUT,i} - k\Gamma_{IN,i}|^2 \right)}}{|k\Gamma_{IN,max}|} \quad (12)$$

A similar judgment can be applied in the case of other modulation schemes, considering the constellation's configuration [21]. The symbols are grouped in clusters (positioned on the same circle) and the normalization constant k is calculated, using all symbols. The inner symbols are projected to the outer circle with respect to each radius ratio, as in (11). The results for five different modulation schemes as shown in Figures 29 to 33 are plotted in Figure 35. EVM was evaluated for 21 frequencies over the 10 GHz band, at 1 Gb/s data-rate, and 10 samples/symbols. As expected, better performances were obtained around the central frequency, with an EVM value of around 2 %. In the 81 – 86 GHz band (allocated by FCC for point-to-point wireless links) the EVM is less than 7.5 % for all modulations.

The implementation of EBG structures enhances bandwidth of microstrip patch antenna; whereas, a metamaterial structure is required for reducing the size of the antenna [22-24]. There is a remarkable increase in the development of wireless communication since the last decade as it is successful in fulfilling the demand for high-speed communication [25]. The demand for upgrading existing technologies has been satisfied by replacing the devices with the new ones. However, there are increased chances of obstacles including power splitter, amplifier, and filter, while improving the capability of related devices [26, 27]. There are major issues faced in the field of Power electronics and drive systems.

Regarding this, many techniques are originated in advance controlling of semi-conductor devices and power electronics to stimulate applications of millimeter wave theory, which can be applied in converters, inverters, power, and utility appliances. Modelling and design of this study will implement the utilization of circuit components in sensors, synchronous motor drives and multi-phase mechanisms [28]. Developments and advantages in adopting millimeter wave identifications will result in reducing the costs of packaging and testing. This instigates an advance growth and developments in the field of electrical engineering which drives the scope of considerations in the wind, energy systems, solar panels, motor hybrid systems and various application of engineering field [29].

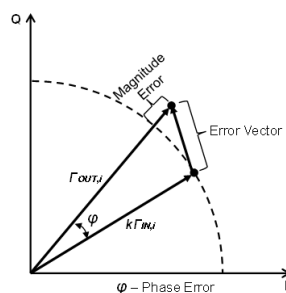


Figure 34. Graphical representation of EVM

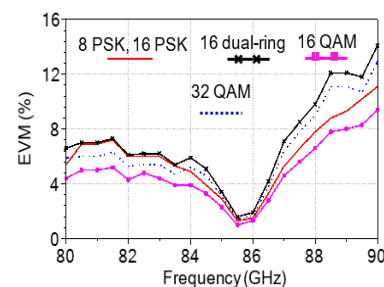


Figure 35. EVM results for various PSK and QAM modulations

#### 4. CONCLUSION

MHMIC six-port interferometer is operating over the 10 GHz band, from 80 to 90 GHz, has been designed and fully characterized using the measurement results from the on die S-parameters. The circuit is designed for use in millimeter wave transceiver front-ends as a quadrature down-converter or direct modulator. Its operating frequency covers millimeter wave point-to-point communications (81-86 GHz) and the spectrum above 85 GHz from imaging systems. The circuit layout uses rounded shapes to improve the S-parameters over a wideband. Two-port measurement results on die are used to build a computer model for realistic system simulations. As known, S-parameter analysis gives an initial estimation of the circuit performances. However, it is not easy for a microwave designer to characterize a six-port simply by using this method because all four outputs are vector combinations of inputs through the circuit. Other analysis tools described in this study make six-port characterization easier. Therefore, a harmonic balance analysis, the evaluation of the qi point, the direct demodulation of the millimeter wave signals (PSK and QAM) and EVM analysis have been performed over the band. This exhaustive analysis demonstrates that the proposed circuit can be used, without any calibration, in a millimeter wave transceiver front-end for modulation schemes up to 32 symbols. This is an important feature, because, due to the circuit's wideband, quasi-optical data-rates can be achieved at low cost, if the circuit is used in wireless communication systems. For both wireless and imaging applications, because the quadrature is maintained with reduced errors over several GHz bandwidths, quadrature down-conversion can be performed directly in millimeter waves. This improves the system performance of heterodyne transceivers over an ultra-wideband when compared to the conventional approach of quadrature down-conversion on the IF or baseband.

#### ACKNOWLEDGEMENTS

The authors would like to acknowledge the Natural Sciences and Engineering Research Council of Canada (NSERC) and of the "Fonds de recherche du Québec – Nature et Technologies" (FRQNT) for the financial support and the Poly-Grames Research Center of "École Polytechnique de Montréal" for MHMIC fabrication.

## REFERENCES

- [1] Li J, Bosisio RG, Wu K. Computer and measurement simulation of a new digital receiver operating directly at millimeter-wave frequencies. *IEEE Transactions on Microwave Theory and Techniques*. 1995 Dec; 43(12):2766-72.
- [2] Hyyrylainen J, Bogod L, Kangasmaa S, Scheck HO, Ylamurto T. Six-port direct conversion receiver. In 1997 27th European Microwave Conference. IEEE, 1997; 1: 341-346.
- [3] Abe M, Sasho N, Brankovic V, Krupezevic D. Direct conversion receiver MMIC based on six-port technology in Proceedings of European Wireless Technology Conference. Paris, France, 2000. 139–142.
- [4] Nasri A, Zairi H, Gharsallah A. A Compact SIW Mixer for Millimeter-Wave Applications. *International Journal of Electrical and Computer Engineering*. 2014 Dec 1; 4(6):902.
- [5] Kumar P. Application of Distribution Power Electronic Transformer for Medium Voltage. *International Journal of Power Electronics and Drive Systems*. 2014 Dec 1; 4(4):547.
- [6] Hentschel T. The Six Port as Communication Receiver. *IEEE Transactions on Microwave Theory and Techniques*. 2005; 53(3): 1039-1047.
- [7] Tatu SO, Moldovan E, Wu K, Bosisio RG, Denidni TA. Ka-band analog front-end for software-defined direct conversion receiver. *IEEE Transactions on Microwave Theory and Techniques*. 2005 Sep; 53(9):2768-76.
- [8] Moldovan E, Tatu SO, Affes S. A 60 GHz multiport front-end architecture with integrated phased antenna array. *Microwave and Optical Technology Letters*. 2008 May; 50(5):1371-6.
- [9] Köelpin A, Vinci G, Laemmle B, Kissinger D, and Weigel R. The Six-Port in Modern Society. *IEEE Microwave Magazine Supplement*. 2010: 35 – 43.
- [10] Tatu SO, Moldovan E, Affes S. Multi-port front-end and transceivers for V-band multi-gigabit/s communication systems. *Digital Front-End in Wireless Communications and Broadcasting Circuits and Signal Processing*. 2011 Sep: 707-32.
- [11] Hannachi C, Hammou D, Djerafi T, Ouairi Z, Tatu SO. Complete characterization of novel MHMICs for V-band communication systems. *Journal of Electrical and Computer Engineering*. 2013; 2013.
- [12] Tatu SO, Serban A, Helaoui M, Koelpin A. Multiport technology: The new rise of an old concept. *IEEE Microwave Magazine*. 2014 Nov; 15(7):S34-44.
- [13] Hannachi C, Tatu SO. A new compact V-band six-port receiver for high data-rate wireless applications. In 2015 IEEE Topical Conference on Wireless Sensors and Sensor Networks (WiSNet). IEEE. 2015: 26-28.
- [14] Moldovan E, Tatu SO. Design and characterization of novel W-band wide-band couplers and six-port circuit. In 2015 European Microwave Conference (EuMC). IEEE. 2015: 279-282.
- [15] Hammou D, Djerafi T, Nedil M, Tatu SO. Considerations for on-wafer millimeter-wave measurements on thin ceramic substrate. *IEEE Transactions on Instrumentation and Measurement*. 2016 Feb; 65(2):441-7.
- [16] [http://cp.literature.agilent.com/litweb/pdf/ads2008/ccsim/ads2008/DataAccessComponent\\_\(Data\\_Access\\_Component\).html](http://cp.literature.agilent.com/litweb/pdf/ads2008/ccsim/ads2008/DataAccessComponent_(Data_Access_Component).html)
- [17] Engen GF, Hoer CA. Application of an arbitrary 6-port junction to power-measurement problems. *IEEE transactions on Instrumentation and Measurement*. 1972 Nov; 21(4):470-4.
- [18] Engen GF. The six-port reflectometer: An alternative network analyzer. *IEEE Transactions on microwave theory and techniques*. 1977 Dec; 25(12):1075-80.
- [19] Engen GF. An improved circuit for implementing the six-port technique of microwave measurements. *IEEE Transactions on microwave theory and techniques*. 1977 Dec; 25(12):1080-3.
- [20] Tatu SO, Moldovan E, Denidni T. Analysis of multipath fading for six-port receiver. *Microwave and Optical Technology Letters*. 2004 Apr 20; 41(2):137-41.
- [21] Hannachi C, Moldovan E, Tatu SO, Ouairi Z. V-band six-port quadrature demodulator: IEEE Error vector magnitude analysis. In Global Symposium on Millimeter-Waves (GSMW). 2015 May 25: 1-3.
- [22] Dewan R, Rahim MK, Hamid MR, Yusoff MF, Majid HA, Esmail BA. Dual band to wideband pentagon-shaped patch antenna with frequency reconfigurability using EBGs. *International Journal of Electrical and Computer Engineering*. 2018 Aug 1; 8(4):2557.
- [23] Lin JF, Chu QX. Enhancing Bandwidth of CP Microstrip Antenna by Using Parasitic Patches in Annular Sector Shapes to Control Electric Field Components. *IEEE Antennas and Wireless Propagation Letters*. 2018 May; 17(5):924-7. doi: 10.1109/LAWP.2018.2825236
- [24] Rothwell EJ, Ouedraogo RO. Antenna miniaturization: definitions, concepts, and a review with emphasis on metamaterials. *Journal of Electromagnetic Waves and Applications*. 2014 Nov 22; 28(17):2089-123.
- [25] Azizi S, El Halaoui M, Kaabal A, Ahyoud S, Asselman A. Enhanced Bandwidth of Band Pass Filter Using a Defected Microstrip Structure for Wideband Application. *International Journal of Electrical and Computer Engineering*. 2018; 8(6):5260-5267.
- [26] Vancl J, Sokol V, Cerny P, Skvor Z. The UWB Amplifier 3.1-10.6 GHz. In 2008 14th Conference on Microwave Techniques 2008 Apr 23: 1-4. IEEE.
- [27] Munir A, Praludi T, Effendi MR. Characterization of Narrowband Hairpin Bandpass Filter Composed of Fractal Koch Geometry. In PIERS Proceedings 2014 Aug 25.
- [28] Prakash G, Balamurugan M, Umashankar S. A new multilevel inverter with reduced number of switches. *International Journal of Power Electronics and Drive Systems (IJPEDS)* 2014; 5 (1): 63-70.
- [29] Xue SJ, Wu W. Scheduling workflow in cloud computing based on hybrid particle swarm algorithm. *TELKOMNIKA Indonesian Journal of Electrical Engineering*. 2012 Nov; 10 (7):1560-6.